Geochemical Perspectives Letters

Carbon isotopic signatures of super-deep diamonds mediated by iron redox chemistry

J. Liu[1*], W. Wang[2*], H. Yang[3], Z. Wu[2,4*], M.Y. Hu[5], J. Zhao[5], W. Bi[5,6], E.E. Alp[5], N. Dauphas[7], W. Liang[8], B. Chen[9], J.-F. Lin[1*]

doi: 10.7185/geochemlet.1915

Abstract

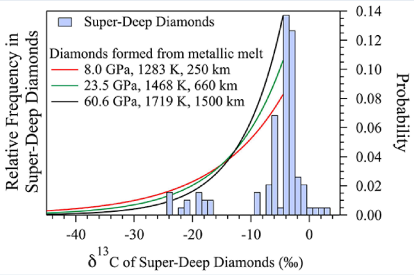

Among redox sensitive elements, carbon is particularly important because it may have been a driver rather than a passive recorder of Earth's redox evolution. The extent to which the isotopic composition of carbon records the redox processes that shaped the Earth is still debated. In particular, the highly reduced deep mantle may be metal-saturated, however, it is still unclear how the presence of metallic phases influences the carbon isotopic compositions of super-deep diamonds. Here we report *ab initio* results for the vibrational properties of carbon in carbonates, diamond, and Fe_3C under pressure and temperature conditions relevant to super-deep diamond formation. Previous work on this question neglected the effect of pressure on the equilibrium carbon isotopic fractionation between diamond and Fe_3C but our calculations show that this assumption overestimates the fractionation by a factor of ~1.3. Our calculated probability density functions for the carbon isotopic compositions of super-deep diamonds derived from metallic melt can readily explain the very light carbon isotopic compositions observed in some super-deep diamonds. Our results therefore support the view that metallic phases are present during the formation of super-deep diamonds in the mantle below ~250 km.

Received 28 May 2018 | Accepted 9 April 2019 | Published 24 May 2019

Introduction

Diamonds are prime recorders of the carbon isotopic compositions of the Earth because some of them are sourced deeply from the longest, isolated regions of Earth's mantle (Cartigny *et al.*, 2014). The $\delta^{13}C$ values (deviations in per mille of $^{13}C/^{12}C$ ratios relative to V-PDB) of natural diamonds show a broad range of variations from -41 ‰ to +3 ‰ with a mode at -5 ± 3 ‰ (Cartigny *et al.*, 2014). Of particular interests are very low $\delta^{13}C$ values of -26 ‰ to -41 ‰ found in some eclogitic and super-deep diamonds (*e.g.*, De Stefano *et al.*, 2009; Smart *et al.*, 2011; Smith *et al.*, 2016). These low $\delta^{13}C$ values are most commonly found in eclogitic diamonds (*e.g.*, Walter *et al.*, 2011), which presumably incorporated a recycled oceanic crust component. It is thus unlikely that these $\delta^{13}C$ values were inherited from Earth's primordial materials. Although eclogitic diamonds with lowest $\delta^{13}C$ values may originate from organic matter at 2.0-2.7 Ga ($\delta^{13}C$ -40 ‰ to -60 ‰) (Smart *et al.*, 2011), such organic matter unlikely survives at the depths (300-1000 km) where super-deep diamonds form (*e.g.*, Anzolini *et al.*, 2019). Isotopic fractionation associated with diamond precipitation from either CH_4 or CO_2-bearing fluids (Galimov, 1991) is also an unlikely explanation for the most negative $\delta^{13}C$ values measured in these diamonds. The reasons are that: (1) the equilibrium fractionation between diamond and CH_4 at mantle temperatures (~+1 ‰) is too low to drive the residual fluid to very negative $\delta^{13}C$ values by Rayleigh distillation; (2) the fractionation between diamond and CO_2 of ~-3 ‰ at mantle temperatures could only produce diamonds whose $\delta^{13}C$ values are ~-8 ‰ or higher. Overall, the question of how some super-deep diamonds acquired highly negative $\delta^{13}C$ values is still open.

1. Department of Geological Sciences, Jackson School of Geosciences, University of Texas at Austin, Austin, Texas 78712, USA
2. Laboratory of Seismology and Physics of Earth's Interior, School of Earth and Space Sciences, University of Science and Technology of China, Hefei, China
3. Center for High Pressure Science and Technology Advanced Research (HPSTAR), Pudong, Shanghai 201203, China
4. CAS Center for Excellence in Comparative Planetology, China
5. Advanced Photon Source, Argonne National Laboratory, Argonne, Illinois 60439, USA
6. Department of Geology, University of Illinois at Urbana-Champaign, Urbana, Illinois 61801, USA
7. Origins Laboratory, Department of the Geophysical Sciences and Enrico Fermi Institute, The University of Chicago, 5734 South Ellis Avenue, Chicago, Illinois 60637, USA
8. Key Laboratory for High Temperature and High Pressure Study of the Earth's Interior, Institute of Geochemistry, Chinese Academy of Sciences, Guiyang, Guizhou 550002, China
9. Hawaii Institute of Geophysics and Planetology, University of Hawaii at Manoa, Honolulu, HI 96822, USA
* Corresponding author (email: jiacliu@utexas.edu; afu@jsg.utexas.edu; wuzq10@ustc.edu.cn; wz30304@mail.ustc.edu.cn)

Through plate tectonics, relatively oxidised iron and carbon species at the Earth's surface are transported to the deep mantle by subducted slabs, where Fe^{2+} can disproportionate into Fe^{3+} and metallic Fe (Equation 1) below ~250 km due to stabilisation of Fe^{3+} in garnet, pyroxene and bridgmanite (Frost *et al.*, 2004; Rohrbach *et al.*, 2007):

$$3FeO = Fe + Fe_2O_3 \quad \text{Eq. 1}$$

The resulting metallic Fe would react with carbonates to form either diamond (Equation 2) or iron carbide (Equation 3), depending on the local Fe:C ratio and thus redox state (Palyanov *et al.*, 2013):

$$FeCO_3 + 2Fe = 3FeO + C \quad \text{Eq. 2}$$

$$FeCO_3 + 5Fe = 3FeO + Fe_3C \quad \text{Eq. 3}$$

Fe_3C can also serve as a reduced C source to form diamonds through the following redox reaction (Bataleva *et al.*, 2016):

$$Fe_3C + 3Fe_2O_3 = 9FeO + C \quad \text{Eq. 4}$$

Moreover, Fe-C alloys/mixtures may melt under the pressure and temperature (*P-T*) conditions of the mantle because of their relatively low melting temperatures, especially in the presence of Ni, as compared to other mantle minerals (*e.g.*, Rohrbach *et al.*, 2014; Liu *et al.*, 2016). The resultant Fe-C melt can form diamonds through the reaction mediated by iron redox chemistry:

$$Fe\text{-}C\ melt + Fe_2O_3 = 3FeO + C \quad \text{Eq. 5}$$

The presence of S or other light elements can significantly lower C solubility in metallic melt and therefore promote diamond formation (Bataleva *et al.*, 2015). For example, Fe-Ni-S-C inclusions have been found in super-deep diamonds (*e.g.*, Kaminsky and Wirth, 2011; Smith *et al.*, 2016). Finding such metallic inclusions requires careful examination as these inclusions are small in size (μm to nm scale) and can be mistaken for graphite (Kaminsky and Wirth, 2011; Smith *et al.*, 2016). The presence of metallic inclusions supports the view that C-bearing metallic melt could serve as a carbon source for some super-deep diamonds below ~250 km.

Horita and Polyakov (2015) have attempted to address the aforementioned question through calculations of the reduced partition function ratio (β-factor) of C in Fe_3C using the heat capacity and the iron phonon density of states (PDOS) at 1 bar. They combined this β-factor with previously published β-factors of diamond and carbonates to calculate the carbon equilibrium isotopic fractionation $\Delta^{13}C$ between these phases,

$$\Delta^{13}C^{B\text{-}A} = 1000(\ln\beta_B - \ln\beta_A) \quad \text{Eq. 6}$$

where A and B are two phases in isotopic equilibrium. An important assumption that Horita and Polyakov (2015) made is that pressure has no effect on this fractionation. However, super-deep diamonds form under high *P-T* conditions in the mantle below 250 km depth, and applied pressure has undoubtedly been shown to stiffen lattice bonds and induce structural and electronic transitions, which in turn can affect β-factors of C in host phases (*e.g.*, Lin *et al.*, 2004, 2012). In order to constrain reliably the extent of C isotopic fractionation during super-deep diamond formation, we used DFT augmented by a Hubbard *U* correction method (Giannozzi *et al.*, 2009) to calculate the β-factors of C in $MgCO_3$, $FeCO_3$, Fe_3C and diamond (Tables S-1, S-2) at the *P-T* conditions of subducted slabs in the mantle. We also measured the PDOS of Fe^{2+} in $FeCO_3$ by nuclear resonant inelastic X-ray scattering (NRIXS) spectroscopy (Dauphas *et al.*, 2018) to evaluate the accuracy of the theoretical calculations.

PDOS of Fe and C in Minerals Relevant to Diamond Formation

The DFT + *U* calculation was verified by comparing the theoretical PDOS of Fe^{2+} in $FeCO_3$ with the one measured by NRIXS (Fig .1). The PDOS results in theory and experiment match well with each other, which could also support the validity of the calculated β-factors of C in carbonates, diamond and nonmagnetic Fe_3C (Fig. S-1). Synchrotron Mössbauer spectra (Fig. S-2) and optical images (Fig. S-3) show that the spin transition of Fe^{2+} in $FeCO_3$ occurs between 44-46 GPa at 300 K. Across the spin transition, the unit cell volume collapses by 9.4 %, the Fe-O bond length is shortened by 4.8 % (Fig. S-4). Meanwhile, the spin transition of iron results in ~5 % decrease of the β-factor of C in LS $FeCO_3$ compared to its HS state (Fig. S-5) as the C-O bound length is lengthened by 2.1 % (Fig. S-4). The magnetic state of Fe_3C changes from ferromagnetic at ambient condition to paramagnetic and finally nonmagnetic at pressures higher than ~22-60 GPa (Lin *et al.*, 2004; Gao *et al.*, 2008). Therefore, nonmagnetic Fe_3C is the relevant phase for most mantle depths. Similar to previous theoretical calculations (Horita and Polyakov, 2015) and C isotopic measurements on natural diamonds and iron carbide inclusions (Mikhail *et al.*, 2014), the magnitude of $\Delta C^{Dia\text{-}Fe_3C}$ is larger than other inter-mineral fractionations involving diamond, such as $\Delta C^{Dia\text{-}Carbonates}$ (Fig. S-6). Our calculated $\Delta C^{Dia\text{-}Fe_3C}$ values along the representative *P-T* conditions of modern mantle and cold slab (Fig. S-6) are as much as 27 % lower than the 1-bar value of $\Delta C^{Dia\text{-}Fe_3C}$ reported by Horita and Polyakov (2015). Therefore the 1-bar data would overestimate the C isotopic fractionation during diamond formation from a Fe_3C source under mantle *P-T* conditions.

Carbon Isotopic Fractionation in Diamonds through Redox Reactions

As discussed by Horita and Polyakov (2015), the most significant reaction that can impart C isotopic fractionation to diamonds is one involving the oxidation of C alloyed with metallic melt to release C to form diamonds (Equation 5). To assess how redox reactions involving Fe-C melt below ~250 km can influence the $\delta^{13}C$ values of super-deep diamonds, we modelled the isotopic fractionation of C between diamond and Fe-C melt. Our calculations accounting for various *P-T* and compositional factors allow us to test whether this diamond formation pathway can account for their $\delta^{13}C$ values.

The C isotopic fractionation can be modelled by using a Rayleigh distillation if the diamonds produced do not back-react with the C source, which is reasonable if the Fe-C source is a melt and the reaction product is a solid characterised by a low self-diffusivity (Koga *et al.*, 2005). As it is challenging to calculate the β-factor of C in Fe-C melt directly, $\Delta^{13}C^{Dia\text{-}FeC\ melt}$ is calculated by the sum of $\Delta^{13}C^{Dia\text{-}Fe_3C}$ (Fig. S-6) and the equilibrium fractionation $\Delta^{13}C^{Fe_3C\text{-}FeC\ melt} = -5.6 \times 10^6/T^2$ anchored to the experimentally determined value of ~-2 ‰ at 6.3 GPa and 1673 K (Reutsky *et al.*, 2015). By using this calculated $\Delta^{13}C^{Dia\text{-}FeC\ melt}$, $\delta^{13}C$ values of diamonds forming from metallic melt can be calculated using a Rayleigh distillation model. Relative to the Fe-C melt source, the diamonds are enriched in the heavy isotope of C. Removal of isotopically heavy diamonds would have driven the Fe-C melt reservoir towards lower $\delta^{13}C$ values and diamonds formed from this low $\delta^{13}C$ reservoir progressively acquired more negative $\delta^{13}C$ values.

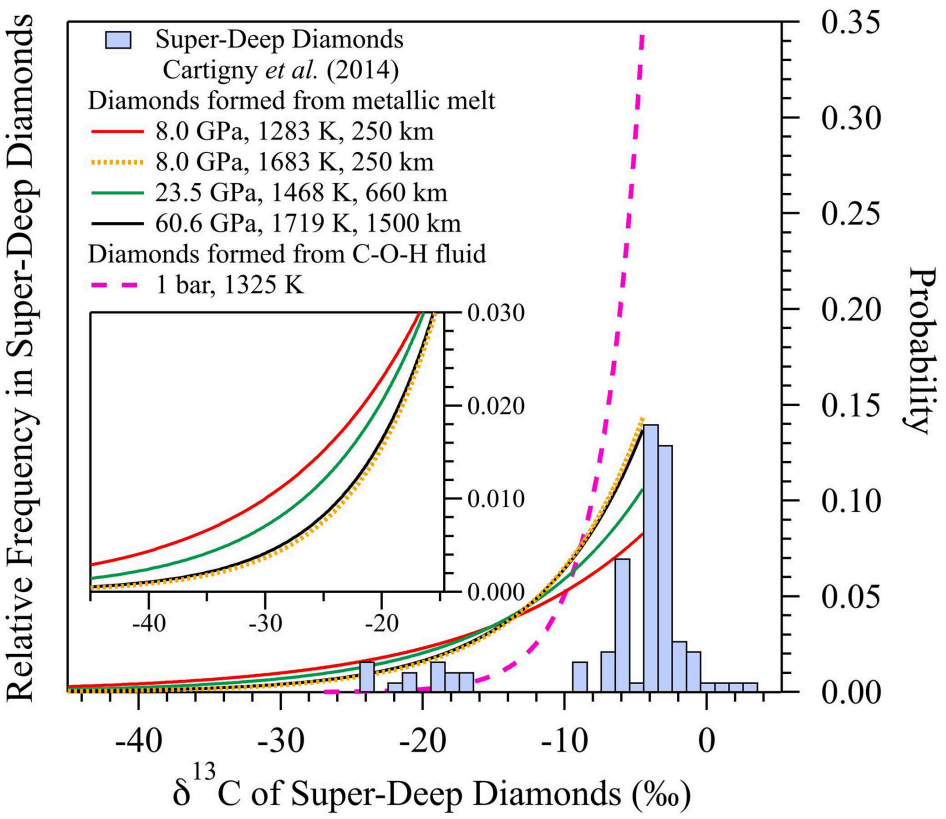

Figure 2 Comparison of the histogram for $\delta^{13}C$ of super-deep diamonds (left axis) and the probability density functions (PDFs, right axis) of $\delta^{13}C^{Dia}$ derived from metallic melt for different *P-T* conditions. The red, green and black solid curves are calculated PDFs by using $\Delta^{13}C^{Dia\text{-}FeC\ melt}$ at 250 km, 660 km and 1500 km depths along a cold slab geotherm (Yang *et al.*, 2017), respectively. The yellow dotted curve is calculated by using $\Delta^{13}C^{Dia\text{-}FeC\ melt}$ at 250 km along the modern mantle geotherm (Yang *et al.*, 2017), which may be similar to the Archean mantle geotherm (Santosh *et al.*, 2010). The pink dashed curve is for diamonds forming from C-H-O fluids, which is calculated using the largest reported value of $\Delta^{13}C^{Dia\text{-}COH}$ (-2.9 ‰) (Cartigny *et al.*, 2014). The inset figure shows the negative tailings of these three PDFs. $\delta^{13}C$ data of super-deep diamonds are from Cartigny *et al.* (2014).

Acknowledgements

W.Z. Wang and Z.Q. Wu acknowledge the Strategic Priority Research Program of the Chinese Academy of Sciences (XDB18000000), the Natural Science Foundation of China (41721002). J.F.L. and N.D. acknowledge support from CSEDI of the NSF Geophysics Program (EAR-1502594). NRIXS experiments used resources of the Advanced Photon Source, a U.S. Department of Energy (DOE) Office of Science User Facility operated for the DOE Office of Science by Argonne National Laboratory under Contract No. DE-AC02-06CH11357. W. Liang acknowledges the National Science Foundation for Young Scientists of China (41802044). W.L. Bi acknowledges COMPRES, the Consortium for Materials Properties Research in Earth Sciences under NSF Cooperative Agreement EAR 1606856. B. Chen acknowledges support from NSF grants EAR-1555388 and EAR-1565708.

Editor: Wendy Mao

Author Contributions

J.C. Liu and W.Z. Wang contributed equally to this work. J.F. Lin, J.C. Liu and W.Z. Wang designed this project; J.C. Liu, H. Yang, N. Dauphas, M.Y. Hu, J.Y. Zhao, W.L. Bi, E.E. Alp, W. Liang and B. Chen performed the experiments and data analysis; W.Z. Wang and Z.Q. Wu performed the calculations; J.C. Liu, W.Z. Wang, N. Dauphas and J.F. Lin wrote the paper.

Additional Information

Supplementary Information accompanies this letter at http://www.geochemicalperspectivesletters.org/article1915.

Cite this letter as: Liu, J., Wang, W., Yang, H., Wu, Z., Hu, M.Y., Zhao, J., Bi, W., Alp, E.E., Dauphas, N., Liang, W., Chen, B., Lin, J.-F. (2019) Carbon isotopic signatures of super-deep diamonds mediated by iron redox chemistry. *Geochem. Persp. Let.* 10, 51–55.

References

Anzolini, C. *et al.* (2019) Depth of diamond formation obtained from single periclase inclusions. *Geology* 47, 219–222.

Bataleva, Y.V., Palyanov, Y.N., Borzdov, Y.M., Bayukov, O.A., Sobolev, N.V. (2015) Interaction of iron carbide and sulfur under P–T conditions of the lithospheric mantle. *Doklady Earth Sciences* 463, 707–711.

pressures up to 61.7 GPa at 300 K. $^{57}FeCO_3$ samples were double-polished to ~20 μm thick and ~40 μm*40 μm in diameter. For nuclear resonance inelastic X-ray scattering (NRIXS) measurements at 12.1 GPa and 21.6 GPa, a DAC with a pair of 400-μm culet diamonds was used, while the upstream diamond was perforated in order to reduce the scattering of income X-ray from the upstream diamond. For the same purpose, one 300-μm mini anvil with a height of about 1 mm together with a normal downstream 300-μm anvil were used for the measurements between 32.0 and 52.5 GPa. The third DAC with a pair of 200-μm diamonds was employed for the measurement at 61.7 GPa. X-ray transparent and high-purity Be gaskets of 3 mm in diameter with cubic boron nitride (c-BN) insert served as sample chamber, which were preindented to ~ 30 μm thick with a hole of ~70 μm in diameter. The pressure medium was mineral oil (Alfa Aesar, 31911) and 5-μm ruby spheres next to the samples were used as pressure gauge. Pressure uncertainty was determined by the pressure shift before and after each NRIXS measurement (Mao *et al.*, 1986). In addition, 1-bar NRIXS measurement was collected from a piece of siderite sample mounted on top of a thin stick.

NRIXS and Synchrotron Mössbauer Spectroscopy (SMS) Measurements and Data Analysis

Both NRIXS and SMS measurements on $^{57}FeCO_3$ were performed at sector 3ID-B of the Advanced Photon Source, Argonne National Laboratory. A monochromatic X-ray beam of ~ 14.4125 keV with 24 bunches separated by 153.4 ns was used to excite the nuclear resonance of the ^{57}Fe nuclei in $FeCO_3$ sample. The NRIXS signals were collected by two avalanche photodiode detectors (APDs) on the side windows of the panoramic cells and a third one in the forward direction. As noticed by recent NRIXS studies (Dauphas *et al.*, 2012, 2014; Liu *et al.*, 2017; Shahar *et al.*, 2016), background removal is critical for deriving robust force constant, which requires long range of energy scan. Therefore, the energy range in our experiments was -160 meV to +170 meV around the nuclear resonance energy of ^{57}Fe for 1-bar measurement and -120 meV to +130 meV for high pressure ones. The energy resolution was 1 meV with a step size of 0.334 meV and a collection time of 3 s/step. Below the pressures of spin transition of Fe^{2+}, 7-12 scans were enough to accumulate 200-350 counts in the strongest inelastic peak. But the inelastic peaks collapsed across the spin transition of Fe^{2+} (Fig. S-8), therefore 14-20 scans were required to achieve good statistics. The complementary synchrotron Mössbauer spectroscopy (SMS) data were collected by the APD in the forward direction (Fig. S-2).

2. First-Principles Calculations

We calculated the vibrational phonon density of state (PDOS) of C in $FeCO_3$, $MgCO_3$, $CaCO_3$, Fe_3C, diamond and the PDOS of Fe in $FeCO_3$ and Fe_3C by an open-source software "Quantum Espresso". It bases on the density functional theory (DFT), plane wave, and pseudopotential (Giannozzi *et al.*, 2009). The calculation details are similar to previous studies (Huang *et al.*, 2013, 2014; Feng *et al.*, 2014; Wu *et al.*, 2015; Wang *et al.*, 2017a,b). The pseudopotentials for C, Fe and Ca are generated using the Vanderbilt method (Vanderbilt, 1990) with the configuration of $2s^22p^2$ and a cutoff radius of 1.3 Bohr for C, the configuration of $3s^23p^63d^{6.5}4s^14p^0$ and a cutoff radius of 1.8 Bohr for Fe, and the configuration $3s^23p^64s^1$ and a cutoff radius of 1.85 Bohr for Ca. The pseudopotential for Mg is generated using the method of von Barth and Car for all channels using a cutoff radius of 2.5 Bohr and five configurations, $3s^23p^0$, $3s^13p^1$, $3s^13p^{0.5}3d^{0.5}$, $3s^13p^{0.5}$, $3s^13d^1$, with weights of 1.5, 0.6, 0.3, 0.3, 0.2, respectively. The pseudopotentials for oxygen is generated using the method of Troullier and Martins (1991) with the configuration $2s^22p^4$ and a cutoff radius of 1.45 Bohr.

All crystal structures are well optimised at various pressures using the method of variable cell shape molecular dynamics (Wentzcovitch, 1991). For $FeCO_3$, $MgCO_3$, $CaCO_3$, Fe_3C and diamond, the electronic states are sampled on a shifted 8×8×8, 8×8×8, 8×8×8, 6×6×6 and 10×10×10, respectively. The plane-wave cutoff energy is 70 Ry and the residual forces converge within 10^{-4} Ry/Bohr. For $MgCO_3$, $CaCO_3$ and diamond, here we adopt the local density approximation (LDA) (Perdew and Zunger, 1981) for exchange correlation functional due to its advantages on calculating structures and thermodynamic properties of minerals (Wentzcovitch *et al.*, 2010; Huang *et al.*, 2013). For Fe-bearing phases, we introduced a Hubbard U correction to the LDA (LDA+U) to sufficiently treat the large on-site Coulomb interactions among Fe 3d electrons. The Hubbard U values were non-empirically calculated using linear response method (Cococcioni and de Gironcoli, 2005) at different pressures. The calculated compression curve and the pressure dependence of Fe-O and C-O bonds match well with previous experimental study (Fig. S-4)

After performing optimisations for all crystal structures, we calculated their phonon frequencies and PDOS using the ab initio lattice dynamics (LD) (Alfè, 2009) method. Mass-dependent equilibrium isotope fractionation factors can be calculated from the changes in vibrational frequencies caused by isotopic substitution of an element in two phases (Bigeleisen and Mayer, 1947; Urey, 1947). Following Richet *et al.* (1977), the reduced partition function ratio β_A of an element X in phase A, which also represents the equilibrium isotope fractionation factor between phase A and atomic X vapor, can be obtained within the harmonic approximation from:

derivation below is to calculate what fraction of the products acquire a given isotopic composition. Statistically, this corresponds to the probability density function (PDF) of the $\delta^{13}C^{Dia}$ values of the instantaneous diamond forming from metallic liquid.

Equation S-5 can be rewritten to express f_C^{Source} as a function of $\delta^{13}C^{Dia}$,

$$f_C^{Source} = \exp[(\delta^{13}C^{Dia} - \delta^{13}C_0^{Source})/ \Delta^{13}C^{Dia\text{-}Source} - 1] \quad \text{Eq. S-6}$$

The corresponding fraction (p) of diamond can be expressed as below:

$$p = 1 - f_C^{Source}$$
$$= 1 - \exp[(\delta^{13}C^{Dia} - \delta^{13}C_0^{Source})/ \Delta^{13}C^{Dia\text{-}Source} - 1] \quad \text{Eq. S-7}$$

If we take $\Delta^{13}C^{Dia\text{-}Source}$ positive, $\delta^{13}C^{Dia}$ starts at $(\delta^{13}C_0^{Source} + \Delta^{13}C^{Dia\text{-}Source})$ at the onset of the reaction and finishes at $-\infty$ when the source is exhausted. The PDF of $\delta^{13}C^{Dia}$, which we note $g(\delta^{13}C^{Dia})$, corresponds to the fraction of diamonds removed dp with isotopic composition between $\delta^{13}C^{Dia}$ and $\delta^{13}C^{Dia} + d\delta^{13}C^{Dia}$, is simply given by (the negative sign is because for positive $\Delta^{13}C^{Dia\text{-}Source}$, $\delta^{13}C^{Dia}$ decreases when p increases),

$$g(\delta^{13}C^{Dia}) = - dp / d\delta^{13}C^{Dia}$$

$$= 1/\Delta^{13}C^{Dia\text{-}Source} \cdot \exp[(\delta^{13}C^{Dia} - \delta^{13}C_0^{Source})/ \Delta^{13}C^{Dia\text{-}Source} - 1] \quad \text{Eq. S-8}$$

We can check that this indeed corresponds to a PDF by calculating the integral,

$$\int_{-\infty}^{\Delta+\delta^{13}C_0^{Source}} g(\delta^{13}C^{Dia})\, d\delta^{13}C^{Dia} = 1 \quad \text{Eq. S-9}$$

The corresponding cumulative distribution function (CDF) is:

$$\text{CDF}\ (\delta^{13}C^{Dia}) = \exp[(\delta^{13}C^{Dia} - \delta^{13}C_0^{Source})/ \Delta^{13}C^{Dia\text{-}Source} - 1] \quad \text{Eq. S-10}$$

The PDF can also be calculated when $\Delta^{13}C^{Dia\text{-}Source} < 0$ but in this case, takes its values between $\delta_0 + \Delta$ and $+\infty$, and the sign of Equation S-8 changes. A general formula that is applicable to both positive and negative values of Δ is therefore,

$$g(\delta^{13}C^{Dia}) = 1/|\Delta^{13}C^{Dia\text{-}Source}| \cdot \exp[(\delta^{13}C^{Dia} - \delta^{13}C_0^{Source})/ \Delta^{13}C^{Dia\text{-}Source} - 1] \quad \text{Eq. S-11}$$

$$\text{CDF}\ (\delta^{13}C^{Dia}) = \exp[(\delta^{13}C^{Dia} - \delta^{13}C_0^{Source})/ |\Delta^{13}C^{Dia\text{-}Source}| - 1] \quad \text{Eq. S-12}$$

Table S-1 Calculated $10^3 \ln\beta$ $^{13/12}$C of carbonates, Fe_3C and diamond along modern mantle and cold slab geotherms (Yang *et al.,* 2017). $10^3 \ln\beta$ of high-spin (HS) and low-spin (LS) $FeCO_3$ are listed in separate columns with spin transition pressure at ~45 GPa.

Depth (km)	P (GPa)	Mantle T (K)	$MgCO_3$	HS $FeCO_3$	LS $FeCO_3$	Fe_3C	Dia	Slab T (K)	$MgCO_3$	HS $FeCO_3$	LS $FeCO_3$	Fe_3C	Dia
200	6.5	1672	8.9	8.8	-	2.1	7.2	1272	15.2	15.1	-	3.8	12.4
216	7.0	1674	8.9	8.8	-	2.1	7.2	1274	15.2	15.1	-	3.8	12.4
231	7.5	1677	8.8	8.8	-	2.1	7.2	1277	15.1	15.0	-	3.8	12.4
246	8.0	1683	8.8	8.7	-	2.1	7.1	1283	15.0	14.9	-	3.8	12.3
260	8.5	1691	8.7	8.7	-	2.1	7.1	1291	14.9	14.8	-	3.7	12.2
275	9.0	1701	8.6	8.6	-	2.1	7.0	1301	14.7	14.6	-	3.7	12.0
289	9.5	1710	8.6	8.5	-	2.1	7.0	1310	14.5	14.4	-	3.6	11.9
303	10.0	1716	8.5	8.5	-	2.1	6.9	1316	14.4	14.3	-	3.6	11.8
318	10.5	1722	8.5	8.5	-	2.1	6.9	1322	14.3	14.2	-	3.6	11.7
332	11.0	1728	8.5	8.4	-	2.1	6.9	1328	14.2	14.1	-	3.6	11.6
346	11.5	1734	8.4	8.4	-	2.1	6.8	1334	14.1	14.0	-	3.6	11.5
360	12.0	1740	8.4	8.3	-	2.1	6.8	1340	14.0	13.9	-	3.5	11.5
373	12.5	1746	8.3	8.3	-	2.0	6.8	1346	13.9	13.9	-	3.5	11.4
387	13.0	1752	8.3	8.3	-	2.0	6.7	1352	13.8	13.8	-	3.5	11.3
401	13.5	1758	8.3	8.2	-	2.0	6.7	1358	13.7	13.7	-	3.5	11.2
414	14.0	1763	8.2	8.2	-	2.0	6.7	1363	13.7	13.6	-	3.5	11.2
428	14.5	1769	8.2	8.1	-	2.0	6.6	1369	13.6	13.5	-	3.4	11.1
441	15.0	1775	8.1	8.1	-	2.0	6.6	1375	13.5	13.4	-	3.4	11.0
455	15.5	1781	8.1	8.1	-	2.0	6.6	1381	13.4	13.3	-	3.4	11.0
468	16.0	1786	8.1	8.0	-	2.0	6.5	1386	13.3	13.2	-	3.4	10.9
481	16.5	1792	8.0	8.0	-	2.0	6.5	1392	13.2	13.2	-	3.4	10.8
494	17.0	1798	8.0	8.0	-	2.0	6.5	1398	13.2	13.1	-	3.4	10.8
507	17.5	1803	8.0	7.9	-	2.0	6.5	1403	13.1	13.0	-	3.3	10.7
520	18.0	1809	7.9	7.9	-	2.0	6.4	1409	13.0	12.9	-	3.3	10.6
533	18.5	1814	7.9	7.9	-	2.0	6.4	1414	12.9	12.8	-	3.3	10.6
546	19.0	1820	7.9	7.8	-	2.0	6.4	1420	12.8	12.8	-	3.3	10.5
559	19.5	1825	7.8	7.8	-	2.0	6.4	1425	12.8	12.7	-	3.3	10.4
571	20.0	1831	7.8	7.8	-	2.0	6.3	1431	12.7	12.6	-	3.3	10.4
584	20.5	1836	7.8	7.7	-	2.0	6.3	1436	12.6	12.6	-	3.3	10.3
596	21.0	1842	7.7	7.7	-	2.0	6.3	1442	12.6	12.5	-	3.3	10.3
609	21.5	1847	7.7	7.7	-	1.9	6.3	1447	12.5	12.4	-	3.2	10.2
621	22.0	1852	7.7	7.6	-	1.9	6.2	1452	12.4	12.4	-	3.2	10.2
634	22.5	1858	7.6	7.6	-	1.9	6.2	1458	12.3	12.3	-	3.2	10.1
646	23.0	1863	7.6	7.6	-	1.9	6.2	1463	12.3	12.2	-	3.2	10.1
658	23.5	1868	7.6	7.6	-	1.9	6.2	1468	12.2	12.2	-	3.2	10.0
670	24.0	1873	7.6	7.5	-	1.9	6.1	1473	12.1	12.1	-	3.2	10.0
682	24.5	1878	7.5	7.5	-	1.9	6.1	1478	12.1	12.0	-	3.2	9.9
694	25.0	1884	7.5	7.5	-	1.9	6.1	1484	12.0	12.0	-	3.2	9.9
705	25.5	1888	7.5	7.4	-	1.9	6.1	1488	12.0	11.9	-	3.1	9.8
716	26.0	1892	7.5	7.4	-	1.9	6.1	1492	11.9	11.9	-	3.1	9.8
728	26.5	1896	7.4	7.4	-	1.9	6.1	1496	11.9	11.8	-	3.1	9.8
739	27.0	1899	7.4	7.4	-	1.9	6.0	1499	11.8	11.8	-	3.1	9.7
751	27.5	1903	7.4	7.4	-	1.9	6.0	1503	11.8	11.8	-	3.1	9.7
762	28.0	1907	7.4	7.4	-	1.9	6.0	1507	11.8	11.7	-	3.1	9.7
773	28.5	1910	7.4	7.3	-	1.9	6.0	1510	11.7	11.7	-	3.1	9.6
784	29.0	1914	7.4	7.3	-	1.9	6.0	1514	11.7	11.6	-	3.1	9.6
795	29.5	1918	7.3	7.3	-	1.9	6.0	1518	11.7	11.6	-	3.1	9.6
806	30.0	1921	7.3	7.3	-	1.9	6.0	1521	11.6	11.6	-	3.1	9.6
817	30.5	1925	7.3	7.3	-	1.9	6.0	1525	11.6	11.5	-	3.1	9.5
827	31.0	1928	7.3	7.3	-	1.9	5.9	1528	11.5	11.5	-	3.1	9.5
838	31.5	1932	7.3	7.3	-	1.9	5.9	1532	11.5	11.5	-	3.1	9.5
849	32.0	1936	7.3	7.2	-	1.9	5.9	1536	11.5	11.4	-	3.1	9.4
859	32.5	1939	7.2	7.2	-	1.9	5.9	1539	11.4	11.4	-	3.1	9.4

869	33.0	1943	7.2	7.2	-	1.9	5.9	1543	11.4	11.4	-	3.1	9.4
880	33.5	1946	7.2	7.2	-	1.9	5.9	1546	11.4	11.3	-	3.1	9.4
890	34.0	1950	7.2	7.2	-	1.9	5.9	1550	11.3	11.3	-	3.1	9.3
900	34.5	1953	7.2	7.2	-	1.9	5.9	1553	11.3	11.3	-	3.1	9.3
910	35.0	1957	7.2	7.1	-	1.9	5.9	1557	11.3	11.2	-	3.0	9.3
923	35.5	1960	7.2	7.1	-	1.9	5.9	1560	11.2	11.2	-	3.0	9.3
935	36.0	1964	7.1	7.1	-	1.9	5.8	1564	11.2	11.2	-	3.0	9.2
947	36.5	1967	7.1	7.1	-	1.9	5.8	1567	11.2	11.1	-	3.0	9.2
959	37.0	1971	7.1	7.1	-	1.9	5.8	1571	11.1	11.1	-	3.0	9.2
971	37.5	1974	7.1	7.1	-	1.9	5.8	1574	11.1	11.1	-	3.0	9.2
983	38.0	1977	7.1	7.1	-	1.9	5.8	1577	11.1	11.0	-	3.0	9.1
995	38.5	1981	7.1	7.1	-	1.9	5.8	1581	11.0	11.0	-	3.0	9.1
1007	39.0	1984	7.1	7.0	-	1.9	5.8	1584	11.0	11.0	-	3.0	9.1
1019	39.5	1988	7.0	7.0	-	1.9	5.8	1588	11.0	11.0	-	3.0	9.1
1031	40.0	1991	7.0	7.0	-	1.9	5.8	1591	10.9	10.9	-	3.0	9.0
1043	40.5	1994	7.0	7.0	-	1.9	5.8	1594	10.9	10.9	-	3.0	9.0
1055	41.0	1998	7.0	7.0	-	1.9	5.7	1598	10.9	10.9	-	3.0	9.0
1067	41.5	2001	7.0	7.0	-	1.9	5.7	1601	10.9	10.8	-	3.0	9.0
1079	42.0	2004	7.0	7.0	-	1.9	5.7	1604	10.8	10.8	-	3.0	9.0
1090	42.5	2008	7.0	6.9	-	1.9	5.7	1608	10.8	10.8	-	3.0	8.9
1102	43.0	2011	6.9	6.9	-	1.9	5.7	1611	10.8	10.8	-	3.0	8.9
1114	43.5	2014	6.9	6.9	-	1.9	5.7	1614	10.7	10.7	-	3.0	8.9
1126	44.0	2017	6.9	6.9	-	1.9	5.7	1617	10.7	10.7	-	3.0	8.9
1137	44.5	2021	6.9	6.9	-	1.9	5.7	1621	10.7	10.7	-	3.0	8.9
1149	45.0	2024	6.9	6.9	6.6	1.9	5.7	1624	10.7	10.7	10.2	3.0	8.8
1161	45.5	2027	6.9	-	6.6	1.9	5.7	1627	10.6	-	10.1	3.0	8.8
1172	46.0	2030	6.9	-	6.5	1.9	5.7	1630	10.6	-	10.1	3.0	8.8
1184	46.5	2034	6.9	-	6.5	1.9	5.6	1634	10.6	-	10.1	3.0	8.8
1195	47.0	2037	6.8	-	6.5	1.9	5.6	1637	10.5	-	10.0	3.0	8.8
1207	47.5	2040	6.8	-	6.5	1.9	5.6	1640	10.5	-	10.0	3.0	8.7
1219	48.0	2043	6.8	-	6.5	1.9	5.6	1643	10.5	-	10.0	3.0	8.7
1230	48.5	2046	6.8	-	6.5	1.9	5.6	1646	10.5	-	10.0	3.0	8.7
1241	49.0	2049	6.8	-	6.5	1.9	5.6	1649	10.4	-	9.9	3.0	8.7
1253	49.5	2053	6.8	-	6.4	1.9	5.6	1653	10.4	-	9.9	2.9	8.7
1264	50.0	2056	6.8	-	6.4	1.9	5.6	1656	10.4	-	9.9	2.9	8.6
1276	50.5	2059	6.8	-	6.4	1.9	5.6	1659	10.4	-	9.9	2.9	8.6
1287	51.0	2062	6.7	-	6.4	1.9	5.6	1662	10.3	-	9.8	2.9	8.6
1298	51.5	2065	6.7	-	6.4	1.9	5.6	1665	10.3	-	9.8	2.9	8.6
1310	52.0	2068	6.7	-	6.4	1.9	5.6	1668	10.3	-	9.8	2.9	8.6
1321	52.5	2071	6.7	-	6.4	1.9	5.6	1671	10.3	-	9.8	2.9	8.5
1332	53.0	2074	6.7	-	6.4	1.9	5.5	1674	10.2	-	9.7	2.9	8.5
1344	53.5	2077	6.7	-	6.4	1.9	5.5	1677	10.2	-	9.7	2.9	8.5
1355	54.0	2080	6.7	-	6.3	1.9	5.5	1680	10.2	-	9.7	2.9	8.5
1366	54.5	2083	6.7	-	6.3	1.9	5.5	1683	10.2	-	9.7	2.9	8.5
1377	55.0	2086	6.7	-	6.3	1.9	5.5	1686	10.1	-	9.6	2.9	8.5
1388	55.5	2089	6.6	-	6.3	1.9	5.5	1689	10.1	-	9.6	2.9	8.4
1399	56.0	2092	6.6	-	6.3	1.9	5.5	1692	10.1	-	9.6	2.9	8.4
1411	56.5	2095	6.6	-	6.3	1.9	5.5	1695	10.1	-	9.6	2.9	8.4
1422	57.0	2098	6.6	-	6.3	1.9	5.5	1698	10.0	-	9.5	2.9	8.4
1433	57.5	2101	6.6	-	6.3	1.9	5.5	1701	10.0	-	9.5	2.9	8.4
1444	58.0	2104	6.6	-	6.2	1.9	5.5	1704	10.0	-	9.5	2.9	8.4
1455	58.5	2107	6.6	-	6.2	1.9	5.5	1707	10.0	-	9.5	2.9	8.3
1466	59.0	2110	6.6	-	6.2	1.9	5.5	1710	10.0	-	9.4	2.9	8.3
1477	59.5	2113	6.6	-	6.2	1.9	5.5	1713	9.9	-	9.4	2.9	8.3
1488	60.0	2116	6.5	-	6.2	1.9	5.4	1716	9.9	-	9.4	2.9	8.3
1499	60.5	2119	6.5	-	6.2	1.9	5.4	1719	9.9	-	9.4	2.9	8.3
1509	61.0	2122	6.5	-	6.2	1.9	5.4	1722	9.9	-	9.4	2.9	8.3
1520	61.5	2125	6.5	-	6.2	1.9	5.4	1725	9.8	-	9.3	2.9	8.3
1531	62.0	2127	6.5	-	6.2	1.9	5.4	1727	9.8	-	9.3	2.9	8.2
1542	62.5	2130	6.5	-	6.2	1.9	5.4	1730	9.8	-	9.3	2.9	8.2
1553	63.0	2133	6.5	-	6.1	1.9	5.4	1733	9.8	-	9.3	2.9	8.2
1563	63.5	2136	6.5	-	6.1	1.9	5.4	1736	9.8	-	9.2	2.9	8.2

1574	64.0	2139	6.5	-	6.1	1.9	5.4	1739	9.7	-	9.2	2.9	8.2
1585	64.5	2142	6.5	-	6.1	1.9	5.4	1742	9.7	-	9.2	2.9	8.2
1596	65.0	2144	6.4	-	6.1	1.9	5.4	1744	9.7	-	9.2	2.9	8.2
1606	65.5	2147	6.4	-	6.1	1.9	5.4	1747	9.7	-	9.2	2.9	8.1
1617	66.0	2150	6.4	-	6.1	1.9	5.4	1750	9.7	-	9.1	2.9	8.1
1627	66.5	2153	6.4	-	6.1	1.9	5.4	1753	9.6	-	9.1	2.9	8.1
1638	67.0	2155	6.4	-	6.1	1.9	5.4	1755	9.6	-	9.1	2.9	8.1
1649	67.5	2158	6.4	-	6.1	1.9	5.4	1758	9.6	-	9.1	2.9	8.1
1659	68.0	2161	6.4	-	6.0	1.9	5.3	1761	9.6	-	9.1	2.9	8.1
1670	68.5	2164	6.4	-	6.0	1.9	5.3	1764	9.6	-	9.0	2.9	8.1
1680	69.0	2166	6.4	-	6.0	1.9	5.3	1766	9.5	-	9.0	2.9	8.0
1691	69.5	2169	6.4	-	6.0	1.9	5.3	1769	9.5	-	9.0	2.9	8.0
1701	70.0	2172	6.4	-	6.0	1.9	5.3	1772	9.5	-	9.0	2.9	8.0

Table S-2 Fitted parameters for the depth-dependence of $10^3 \ln\beta^{13}/^{12}C$ of major carbon species along geotherms of modern mantle and cold slab (Yang *et al.*, 2016). ($10^3 \ln\beta^{13}/^{12}C = a_0 + a_1x + a_2x^2 + a_3x^3$, where x is depth in km). The pressure of Fe^{2+} spin transition in $FeCO_3$ is set to 45 GPa, corresponding to 1150 km.

Slab	a_0	a_1	a_2	a_3
Fe_3C	4.269(4)	-2.64(3)e^{-3}	1.84(4)e^{-6}	-4.6(6)e^{-10}
HS $FeCO_3$	17.3(1)	-1.15(3)e^{-2}	6.5(4)e^{-6}	-1.3(2)e^{-9}
LS $FeCO_3$	14.2(1)	-4.73(1)e^{-3}	1.217(6)e^{-6}	-1.38(1)e^{-10}
$MgCO_3$	17.46(3)	-1.19(1)e^{-2}	7.1(1)e^{-6}	-1.70(4)e^{-9}
Diamond	14.29(3)	-9.86(9)e^{-3}	6.1(1)e^{-6}	-1.48(3)e^{-9}
Normal Mantle	a_0	a_1	a_2	a_3
Fe_3C	2.340(4)	-1.06(2)e^{-3}	8.0(2)e^{-7}	-1.99(6)e^{-10}
HS $FeCO_3$	9.64(1)	-4.19(4)e^{-3}	1.58(3)e^{-6}	0
LS FeCO3	8.254(1)	-1.769(2)e^{-3}	2.630(8)e^{-7}	0
$MgCO_3$	9.85(1)	-5.09(5)e^{-3}	3.01(5)e^{-6}	-7.3(2)e^{-10}
Diamond	7.99(1)	-4.22(4)e^{-3}	2.64(5)e^{-6}	-6.4(2)e^{-10}

Supplementary Figures

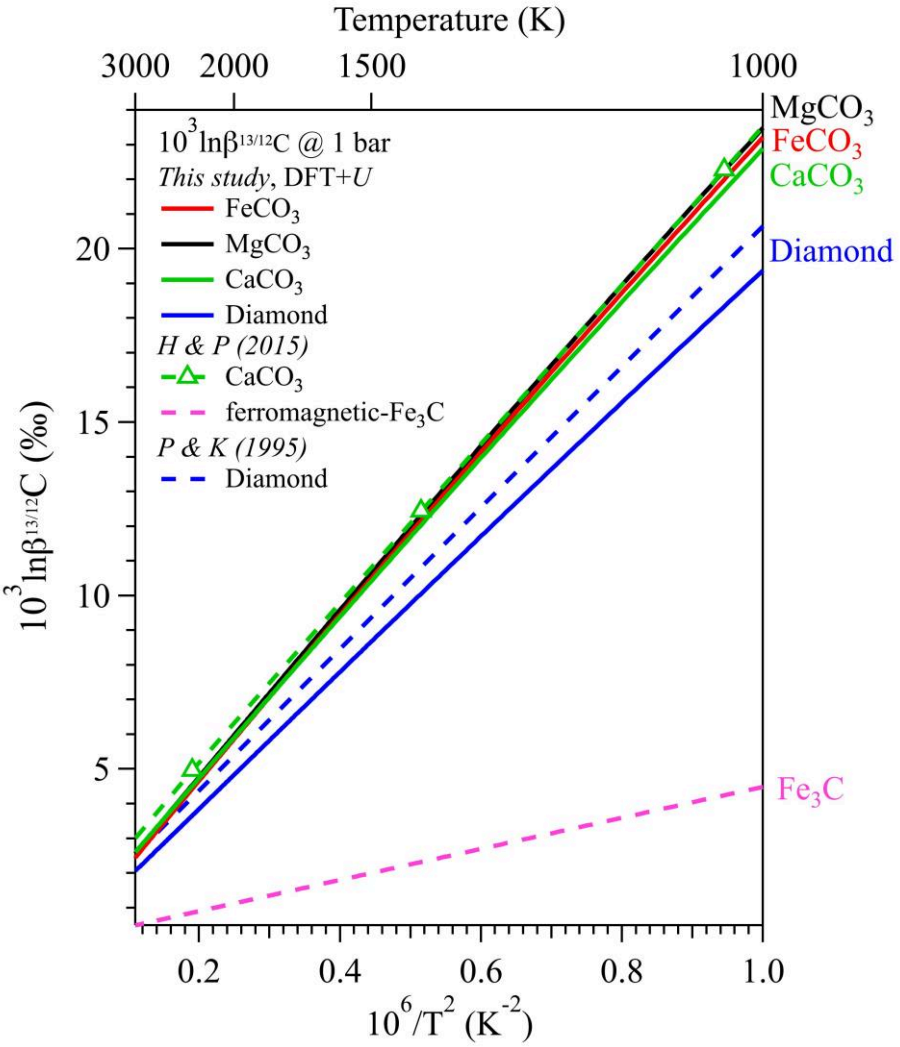

Figure S-1 The 1-bar $^{13}C/^{12}C$ β-factors of major C-bearing minerals. The solid curves are for $FeCO_3$ (red), $MgCO_3$ (black), $CaCO_3$ (green) and diamond (blue) calculated by this study. The green dashed curve with open triangles for $CaCO_3$ and the pink dashed curve for ferromagnetic-Fe_3C are calculated by Horita and Polyakov (2015). The blue dashed curve for diamond is calculated by Polyakov and Kharlashina (1995).

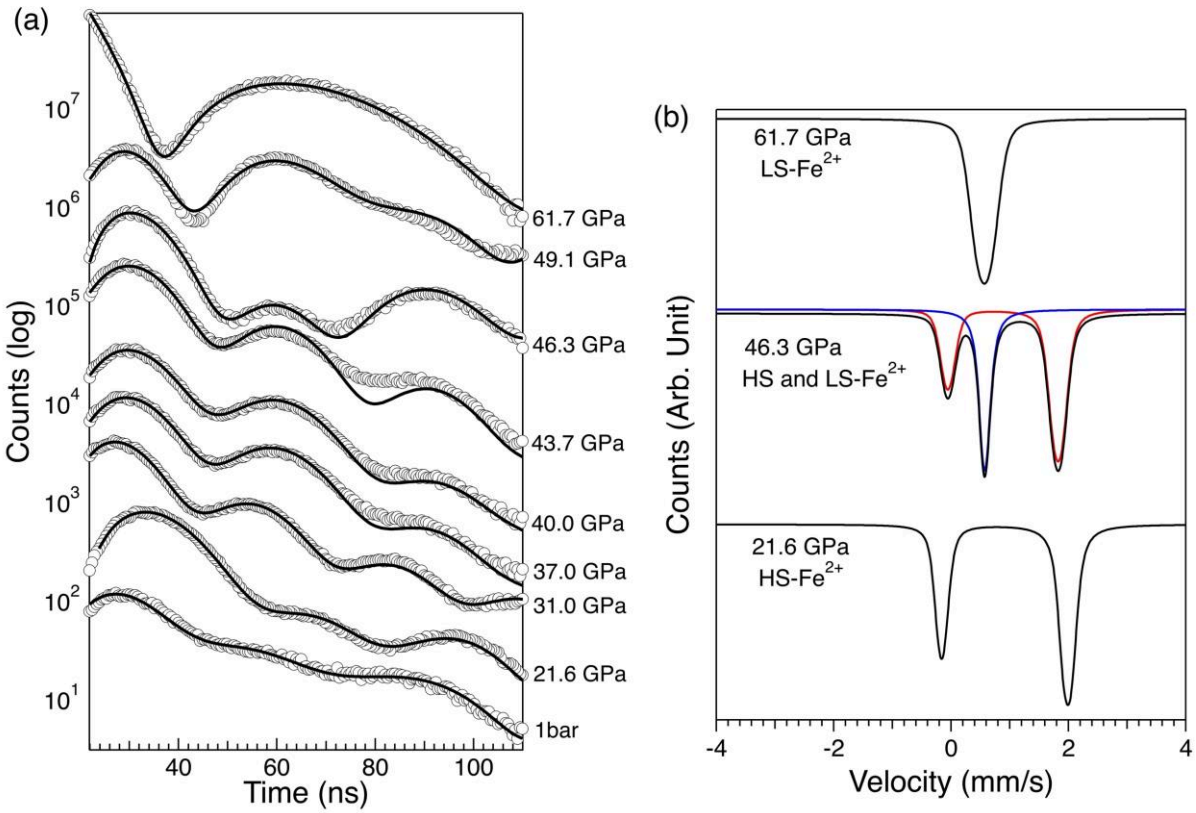

Figure S-2 Synchrotron Mössbauer spectra (SMS) of $FeCO_3$ showing spin transition of Fe^{2+} between 43-46 GPa and 300 K. **(a)** SMS of $FeCO_3$ collected at 1 bar to 61.7 GPa and 300 K. The white cycles are raw data and black curves are the fitting curves. **(b)** Representative energy-domain spectra calculated from the fitting results of the SMS spectra by CONUSS (Sturhahn, 2000). Before the spin transition, a doublet is used to fit the spectra, and the asymmetry is likely due to polarisation of the synchrotron Mössbauer source (Cerantola *et al.*, 2015); a double (red) and a singlet (blue) are employed to fit the SMS spectra within the spin transition pressures; a singlet is used for spectra at pressures higher than the spin transition pressure (~46 GPa).

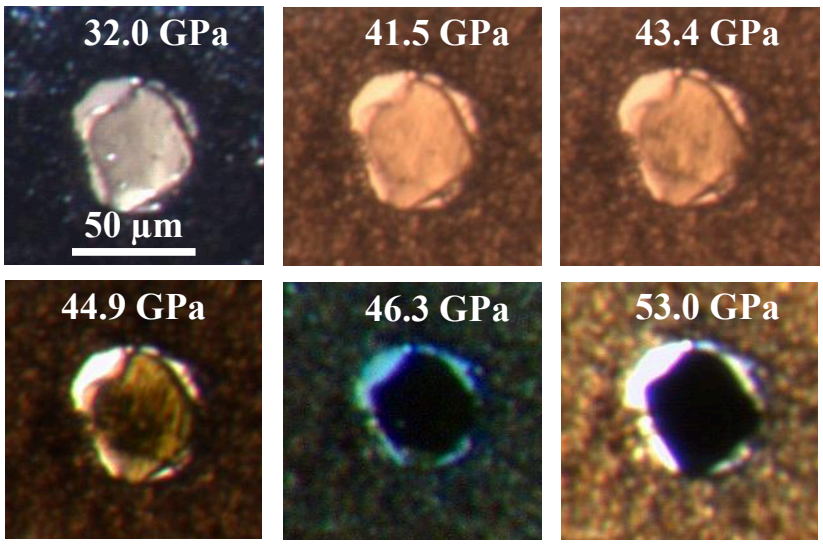

Figure S-3 The $FeCO_3$ sample in a diamond anvil cell transforms from transparent to opaque between 43.4 and 46.3 GPa, indicating a transition of Fe^{2+} from high-spin state (1 bar – 43.4 GPa) to mixed-spin state (43.4–46.3 GPa) and finally to low-spin state (>46.3 GPa).

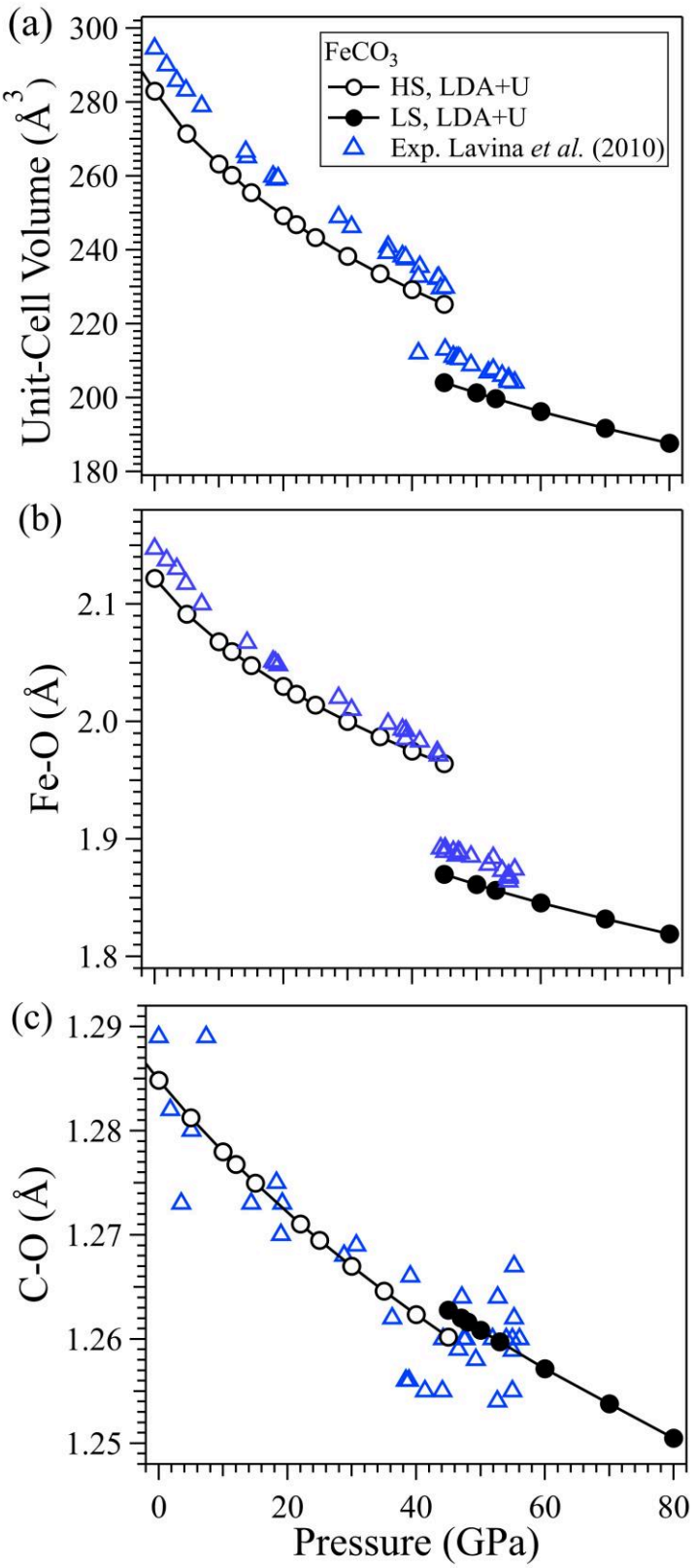

Figure S-4 Pressure-dependence of unit-cell volume **(a),** the average lengths of Fe-O bonds **(b)** and C-O bonds **(c)** in $FeCO_3$. The open and filled circles with fitting curves are for high-spin and low-spin states of Fe^{2+}, respectively, which are calculated using DFT+*U* by this study; the open blue triangles are experimental results from single-crystal XRD measurements (Lavina *et al*., 2010).

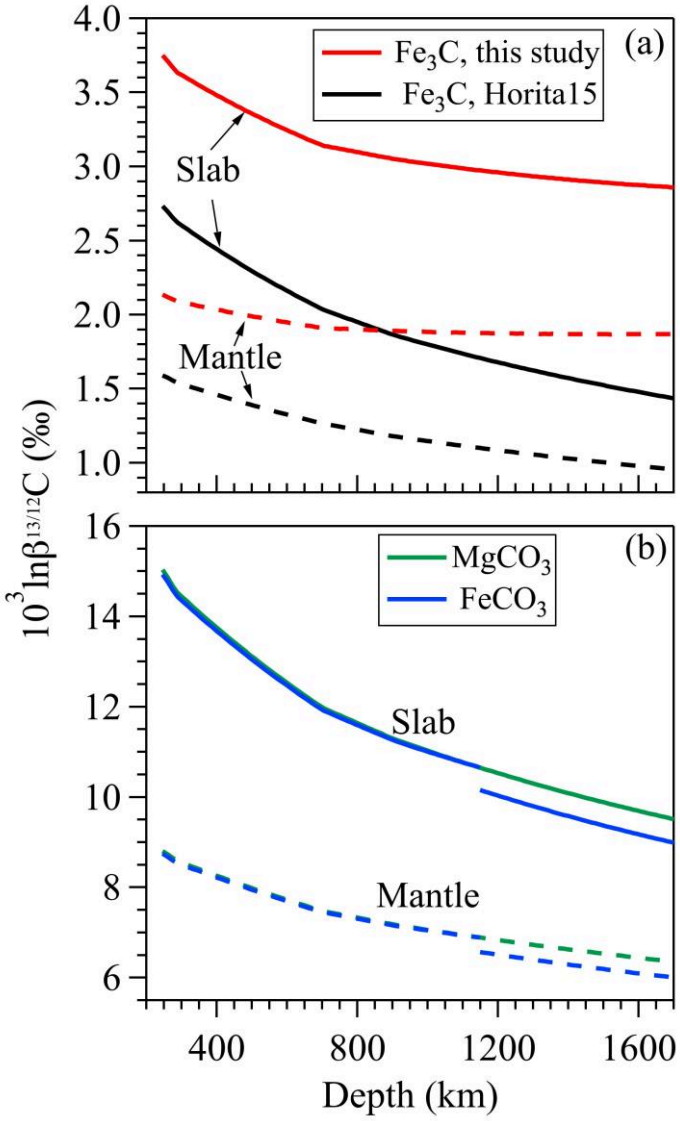

Figure S-5 The $^{13}C/^{12}C$ β-factors of Fe_3C (red curves), $MgCO_3$ (green curves) and $FeCO_3$ (blue curves by this study; Fe_3C by Horita and Polyakov (2015, black curves, only temperature effect is considered) along geotherms (Yang *et al.*, 2017) of modern mantle (dashed curves) and cold slab (solid curves). The discontinuities in $FeCO_3$ curves are caused by spin transition of Fe^{2+}.

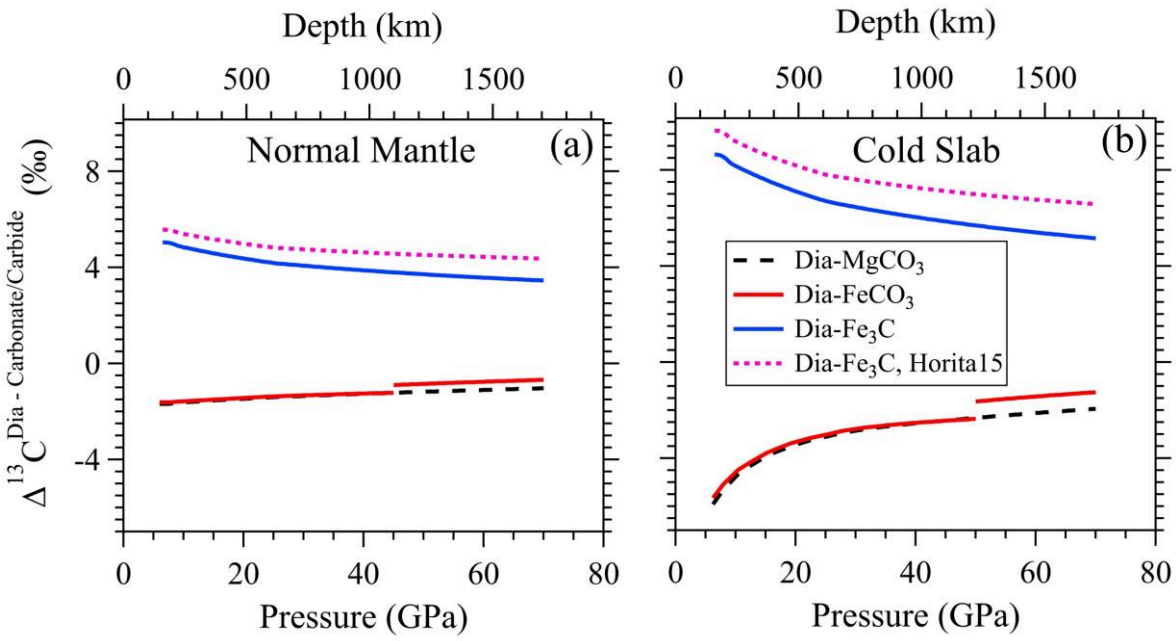

Figure S-6 Equilibrium $^{13}C/^{12}C$ isotopic fractionation between diamond and sourcing carbonate/carbide along modern mantle geotherm **(a)**, and cold slab geotherm **(b)** (Yang *et al*., 2017). As the Archean mantle geotherm may be comparable with current normal geotherm (Santosh *et al*., 2010), (b) may be also applicable for Archaean diamonds. The discontinuity for $\Delta^{13}C^{Dia\text{-}FeCO_3}$ (red curves) around 50 GPa is due to spin transition of Fe^{2+} in $FeCO_3$. The black dashed curves are for $\Delta^{13}C^{Dia\text{-}MgCO_3}$. Pressure-driven magnetic and spin transitions in Fe_3C makes the non-magnetic state stable in most parts of the mantle (Lin *et al*., 2004; Gao *et al*., 2008), therefore only non-magnetic Fe_3C (blue curves) is considered here. For the pink dotted curves, 1-bar $^{13}C/^{12}C$ β-factors of Fe_3C reported by Horita and Polyakov (2015) are used for calculating $\Delta^{13}C^{Dia\text{-}Fe_3C}$ with only temperature effect but no pressure correction.

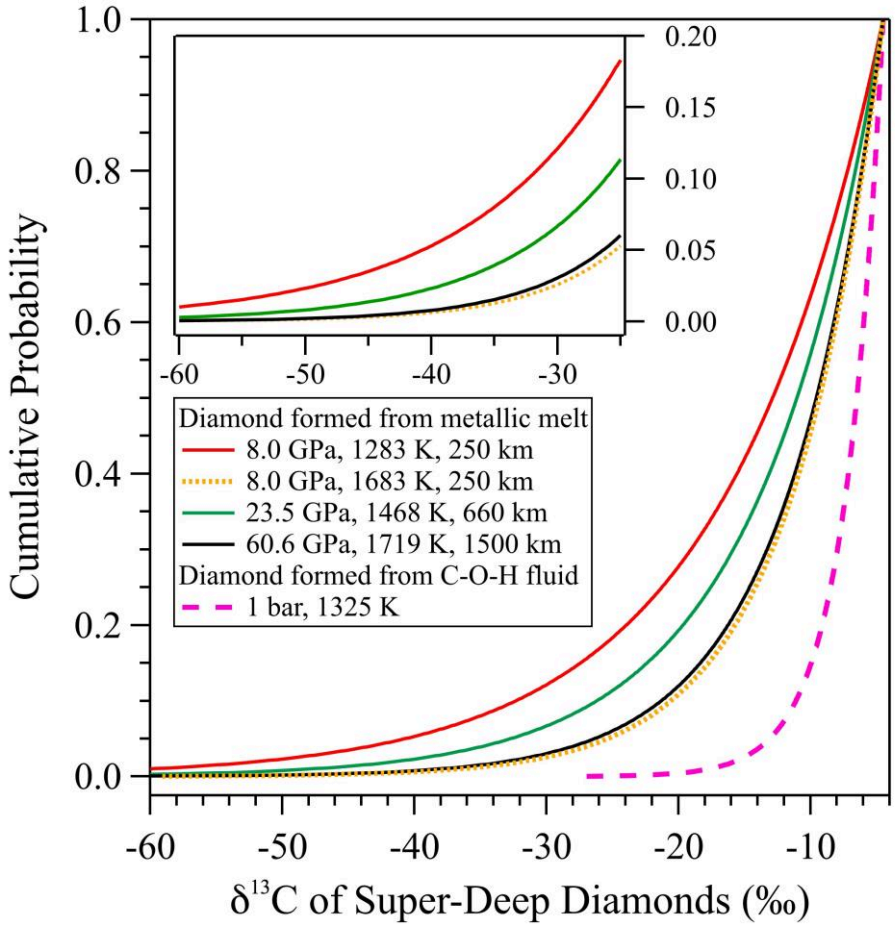

Figure S-7 The cumulative distribution functions (CDFs) of $\delta^{13}C$ of super-deep diamonds forming from a Fe-C melt source. The red, green and black solid curves are CDFs at depths 250 km, 660 km and 1500 km depths along cold slab geotherm (Yang *et al.*, 2017), respectively. The yellow dotted curve is calculated by using $\Delta^{13}C^{Dia\text{-}FeC}$ melt at 250 km along modern mantle geotherm (Yang *et al.,* 2017). The pink dashed curve is for diamonds forming from C-O-H fluid (Cartigny *et al.*, 2014). The inset figure shows the CDFs for $\delta^{13}C$ of diamonds ranging from -60 ‰ to -25 ‰.

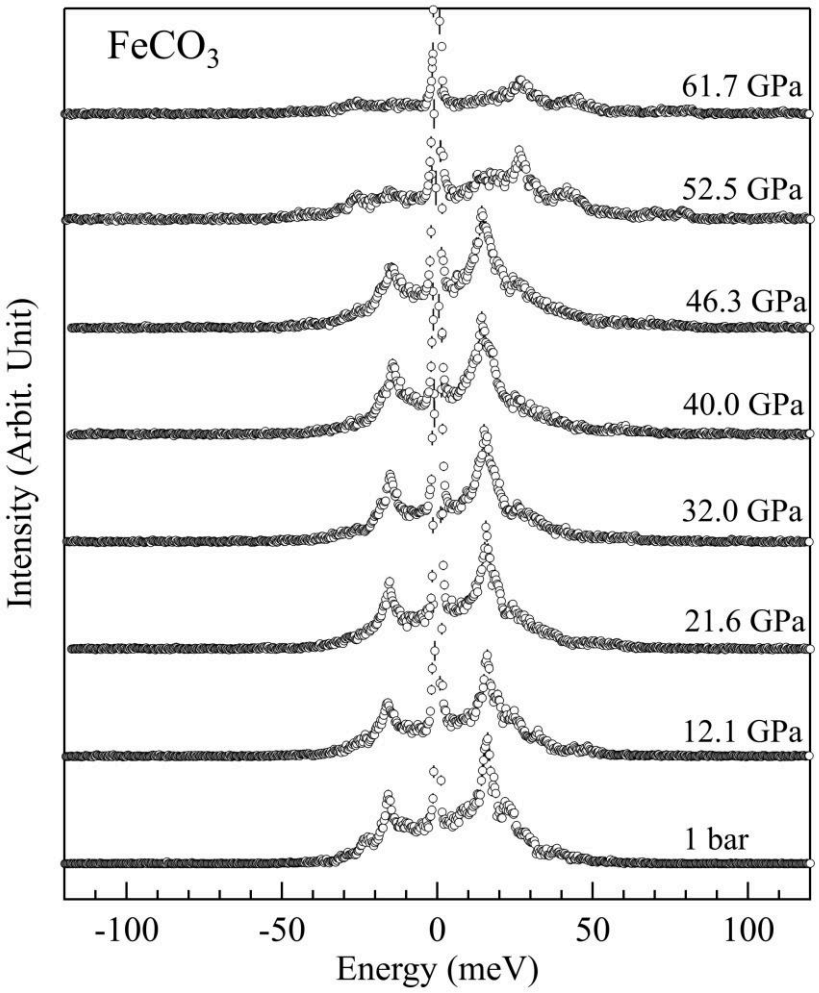

Figure S-8 Nuclear resonant inelastic X-ray scattering (NRIXS) spectra of $FeCO_3$ up to 61.3 GPa and 300 K. Significant changes in inelastic peaks happens around 46 GPa as a result of spin transition of Fe^{2+}.

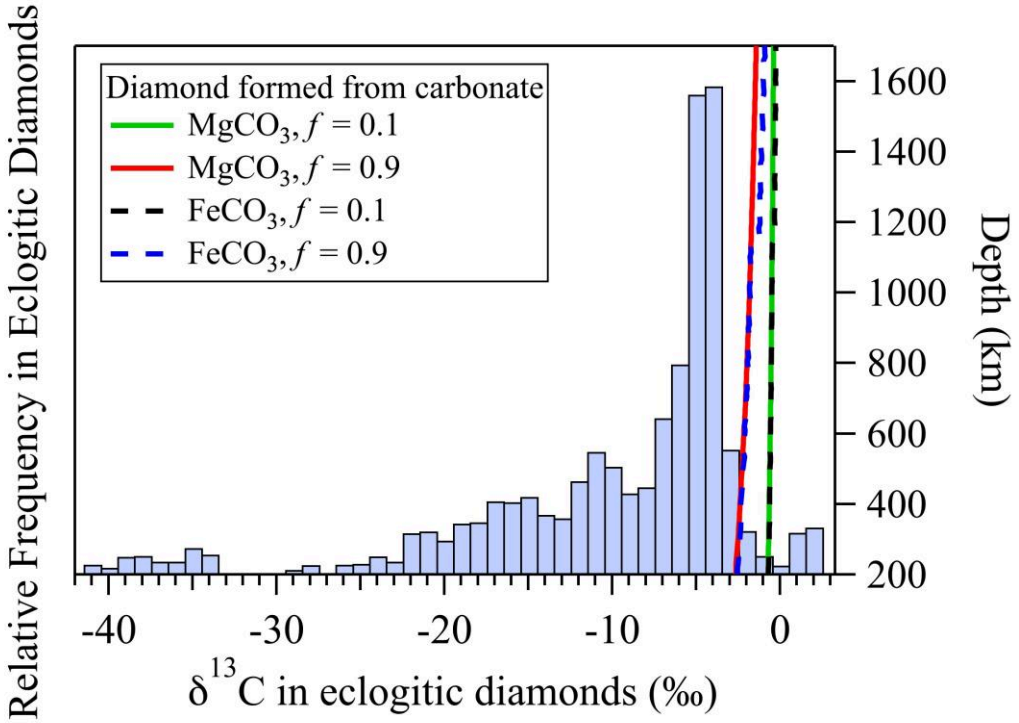

Figure S-9 A comparison between the distribution of $\delta^{13}C$ of eclogitic diamonds and $\delta^{13}C$ of diamonds forming from carbonate sources at depths. The histogram for $\delta^{13}C$ of eclogitic diamonds (Cartigny *et al*., 2014) plotted to the left axis; calculated $\delta^{13}C$ of diamonds as a function of depths from reduction of $MgCO_3$ (solid curves) and $FeCO_3$ (dashed curves) with initial $\delta^{13}C$ as 0 ‰ plotted to the right axis. The C isotopic fractionation between solids is calculated by using a Rayleigh distillation model with the conservation of bulk $\delta^{13}C$ (Eq. S-4 in SI text) along an expected geotherms of modern mantle and cold slab (Yang *et al.*, 2017), respectively. The residual C fraction (*f*) in $MgCO_3$ or $FeCO_3$ is 0.1 for the green solid and black dashed curves; *f* equals 0.9 for the red solid and blue dashed curves.

Supplementary Information References

Alfè, D. (2009) PHON: A program to calculate phonons using the small displacement method. *Computer Physics Communications* 180, 2622–2633.

Bigeleisen, J., Mayer, M.G. (1947) Calculation of Equilibrium Constants for Isotopic Exchange Reactions. *The Journal of Chemical Physics* 15, 261.

Cerantola, V. *et al.* (2015) High-pressure spectroscopic study of siderite ($FeCO_3$) with a focus on spin crossover. *American Mineralogist* 100, 2670–2681.

Cococcioni, M., de Gironcoli, S. (2005) Linear response approach to the calculation of the effective interaction parameters in the LDA+U method. *Physical Review B* 71, 035105.

Dauphas, N. *et al.* (2012) A general moment NRIXS approach to the determination of equilibrium Fe isotopic fractionation factors: Application to goethite and jarosite. *Geochimica et Cosmochimica Acta* 94, 254–275.

Dauphas, N. *et al.* (2014) Magma redox and structural controls on iron isotope variations in Earth's mantle and crust. *Earth and Planetary Science Letters* 398, 127–140.

Feng, C., Qin, T., Huang, S., Wu, Z., Huang, F. (2014) First-principles investigations of equilibrium calcium isotope fractionation between clinopyroxene and Ca-doped orthopyroxene. *Geochimica et Cosmochimica Acta* 143, 132–142.

Giannozzi, P. *et al.* (2009) QUANTUM ESPRESSO: a modular and open-source software project for quantum simulations of materials. *Journal of Physics: Condensed Matter* 21, 395502.

Horita, J., Polyakov, V.B. (2015) Carbon-bearing iron phases and the carbon isotope composition of the deep Earth. *Proceedings of the National Academy of Sciences* 112, 31–36.

Huang, F., Chen, L., Wu, Z., Wang, W. (2013) First-principles calculations of equilibrium Mg isotope fractionations between garnet, clinopyroxene, orthopyroxene, and olivine: Implications for Mg isotope thermometry. *Earth and Planetary Science Letters* 367, 61–70.

Huang, F., Wu, Z., Huang, S., Wu, F. (2014) First-principles calculations of equilibrium silicon isotope fractionation among mantle minerals. *Geochimica et Cosmochimica Acta* 140, 509–520.

Krissansen-Totton, J., Buick, R., Catling, D.C. (2015) A statistical analysis of the carbon isotope record from the Archean to Phanerozoic and implications for the rise of oxygen. *American Journal of Science* 315, 275–316.

Liang, W. *et al.* (2018) Single crystal growth, crystalline structure investigation and high-pressure behavior of impurity-free siderite ($FeCO_3$). *Physics and Chemistry of Minerals* 1–12.

Liu, J. *et al.* (2017) Iron isotopic fractionation between silicate mantle and metallic core at high pressure. *Nature Communications* 8, ncomms14377.

Mao, H. -k., Xu, J., Bell, P.M. (1986) Calibration of the Ruby Pressure Gauge to 800 kbar Under Quasi-Hydrostatic Conditions. *Journal of Geophysical Research* 91, 4673–4676.

Perdew, J.P., Zunger, A. (1981) Self-interaction correction to density-functional approximations for many-electron systems. *Physical Review B* 23, 5048–5079.

Polyakov, V.B., Kharlashina, N.N. (1995) The use of heat capacity data to calculate carbon isotope fractionation between graphite, diamond, and carbon dioxide: a new approach. *Geochimica et Cosmochimica Acta* 59, 2561–2572.

Richet, P., Bottinga, Y., Javoy, M. (1977) A Review of Hydrogen, Carbon, Nitrogen, Oxygen, Sulphur, and Chlorine Stable Isotope Fractionation Among Gaseous Molecules. *Annual Review of Earth and Planetary Sciences* 5, 65–110.

Shahar, A., Schauble, E.A., Caracas, R., Gleason, A.E., Reagan, M.M., Xiao, Y., Shu, J., Mao, W. (2016) Pressure-dependent isotopic composition of iron alloys. *Science* 352, 580–582.

Sturhahn, W. (2000) CONUSS and PHOENIX: Evaluation of nuclear resonant scattering data. *Hyperfine Interactions* 125, 149–172.

Troullier, N., Martins, J.L. (1991) Efficient pseudopotentials for plane-wave calculations. II. Operators for fast iterative diagonalization. *Physical Review B* 43, 8861–8869.

Urey, H.C. (1947) The thermodynamic properties of isotopic substances. *Journal of the Chemical Society (Resumed)* 562.

Vanderbilt, D. (1990) Soft self-consistent pseudopotentials in a generalized eigenvalue formalism. *Physical Review B* 41, 7892–7895.

Wang, W., Qian, T., Zhou, C., Huang, S., Wu, Z., Huang, F. (2017a) Concentration effect on equilibrium fractionation of Mg-Ca isotopes in carbonate minerals: Insights from first-principles calculations. *Geochimica et Cosmochimica Acta* 208, 185–197.

Wang, W., Zhou, C., Qin, T., Kang, J., Huang, S., Wu, Z., Huang, F. (2017b) Effect of Ca content on equilibrium Ca isotope fractionation between orthopyroxene and clinopyroxene. *Geochimica et Cosmochimica Acta*. Elsevier Ltd 219, 44–56.

Wentzcovitch, R.M. (1991) Invariant molecular-dynamics approach to structural phase transitions. *Physical Review B* 44, 2358–2361.

Wentzcovitch, R.M., Yu, Y.G., Wu, Z. (2010) Thermodynamic Properties and Phase Relations in Mantle Minerals Investigated by First Principles Quasiharmonic Theory. *Reviews in Mineralogy and Geochemistry* 71, 59–98.

Wu, Z., Huang, F., Huang, S. (2015) Isotope fractionation induced by phase transformation: First-principles investigation for Mg_2SiO_4. *Earth and Planetary Science Letters* 409, 339–347.

Yang, D., Wang, W., Wu, Z. (2017) Elasticity of superhydrous phase B at the mantle temperatures and pressures: Implications for 800 km discontinuity and water flow into the lower mantle. *Journal of Geophysical Research: Solid Earth* 122, 5026–5037.